Spatio-temporal structure extraction and denoising of geophysical fluid image sequences using 3D curvelet transforms

Jianwei Ma, Olivier Titaud, Arthur Vidard, François-Xavier Le Dimet

INRIA

Spatio-temporal structure extraction and denoising of geophysical fluid image sequences using 3D curvelet transforms

Jianwei Ma — Olivier Titaud — Arthur Vidard — François-Xavier Le Dimet

N° 6683

Octobre 2008

Thème NUM

Rapport de recherche

Spatio-temporal structure extraction and denoising of geophysical fluid image sequences using 3D curvelet transforms

Jianwei Ma* , Olivier Titaud † , Arthur Vidard†, François-Xavier Le Dimet†

Abstract: Since several decades many satellites have been launched for the observation of the Earth for a better knowledge of the atmosphere and of the ocean. The sequences of images that such satellites provide show the evolution of some large scale structures such as vortices and fronts. It is obvious that the dynamic of these structures may have a strong predictive potential. Extracting these structures and tracking their evolution automatically is then essential for future forecast systems. In this paper we consider extraction of spatio-temporal geometric structures from image sequences of geophysical fluid flow using three-dimensional (3D) curvelet transform and total variation minimization. Numerical experiments on simulated geophysical fluids and real video data by remote sensing show good performances of the proposed method in terms of denoising and edge structural extraction. This work is partially motivated by a sequent application to image sequence assimilation of geophysical fluids.

Key-words: 3D Curvelets, feature extraction, 3D total variation, data assimilation, video/image sequences, remote sensing

* School of Aerospace, Tsinghua University, Beijing 100084, China. E-mail: jma@tsinghua.edu.cn
† INRIA, Lab. Jean-Kuntzmann, BP 53, 38041 Grenoble Cedex 9, France. E-mail: Francois-Xavier.Le-Dimet@imag.fr, Olivier.Titaud@imag.fr, Arthur.Vidard@imag.fr

Extraction de structures spatio-temporelle et débruitage de séquences d'image de fluides géophysiques à l'aide de transformées de courbelettes 3D

Résumé : Depuis quelques décénies de nombreux satellites d'observation de la terre ont été lancésafin d'améliorer nos connaissances de l'atmosphère et de l'océan. Les séquences d'image fournies par de tels satellites montrent l'évolution de structures grandes échelles telles que les syclones et les fronts. Il est évident que la dynamique contenue dans ces structures peuvent avoir un fort potentiel prédictif. Extraire ces structures et suivre leur évolution de façon automatique est donc essentiel pour les futurs systèmes de prévision. Dans cet article on considère l'extraction de structures géometriques spatio-temporelles dans des séquences d'images de fluides géophysiques en utilisant des transformées en coubelettes 3D une minimisation de la variation totale. Des expériences numériques sur des images de fluides géophysiques simulées et des données de vidéo réelles montrent la bonne performance de la méthode proposée en terme de débruitage et extraction de structure.

Mots-clés : Courbelettes 3D , extraction de caractéristiques, Total Variation 3D, assimilation de données, video/séquences d'image, télédetection
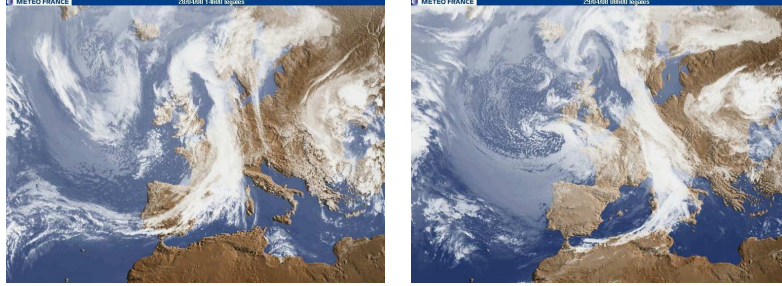
Figure 1: Image sequence over Europe provided by the METEOSAT satellite (visible channel, source Météo France).
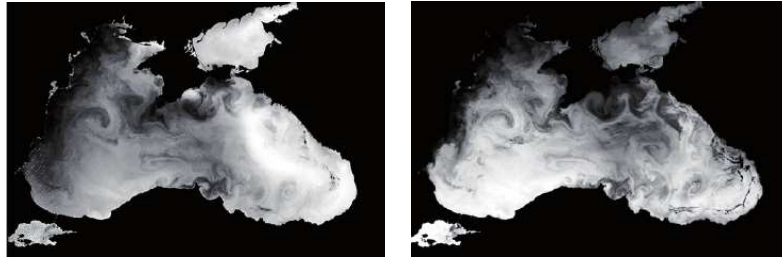

Figure 2: Images of sea surface temperature of the Black Sea provided by the AVHRR satellite (infra-red channel, source NOAA).

1 Introduction

1.1 Background

Current weather and ocean forecast systems assimilate [1, 2] in-situ or remote measurements of the state variables of the modeled flow such as winds, pressure, temperature, salinity,... in order to estimate initial conditions. Since several decades many satellites have been launched for the observation of the Earth for a better knowledge of the atmosphere and of the ocean. Geostationary or polar orbiting Earth observation satellites provide image sequences which clearly show the evolution of large scale features such as fronts, edges shapes of vortices and their trajectory (see Fig. 1 and 2).

Unfortunately, this kind of information are not yet taken into account in a quantitative way by the operational forecast centers. However the evolution of these structures have a strong predictive potential because they may give some information about the dynamic of the underlying physical system.

Extracting and tracking fluid structures from geophysical image sequences could prove very valuable in the framework of Image Sequences Assimilation (ISA). Indeed, the later aim at improving forecast systems by taking into account dynamical informations contained in the structure evolution that satellite images provide [24, 3, 23].

In the prior work [4], we applied curvelet transform [6, 7] to the detection and tracking of characteristic deformable structures in some geophysical fluid
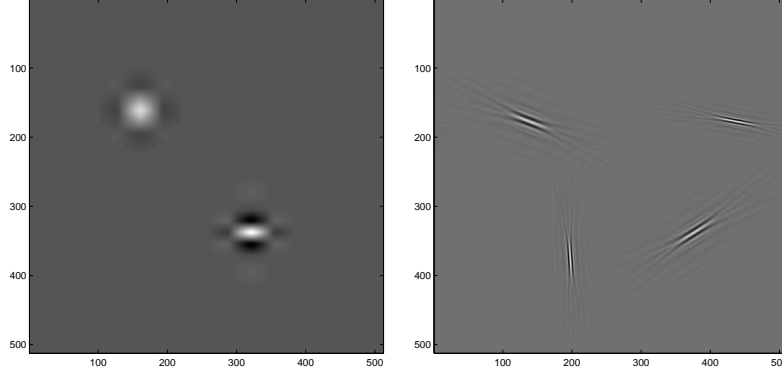
Figure 3: The elements of wavelets (left) and curvelets on various scales, directions and translations in the spatial domain (right).

flow images. In this paper we present extraction of spatio-temporal structures from similar geophysical fluid image sequences using 3D curvelet transform .

1.2 Motivation

Although applications of wavelets to extraction and analysis of geophysical fluid images have become increasingly popular (see e.g. [29,30,31,32,33,34] among lots of literature), traditional wavelets ignore the geometric properties of structures and do not exploit the regularity of edges : they are efficient to represent point singularities only. Therefore, wavelet-based structure extraction and denoising becomes computationally inefficient for geometric features with 2D line and 3D surface singularities. Moreover discrete wavelet thresholding could lead to oscillations along edges.

The curvelet transform was proposed by Candès *et al.* [5, 6, 7, 8]. It is a new geometric wavelet transform. The 2D curvelet transform allows an optimal sparse representation of objects with C^2-singularities. In comparison with wavelets, curvelets show better performances for the analysis of line-singularities. Thus curvelet seems to be more adapted to extract edges and then structures. For a smooth object f with discontinuities along C^2-continuous curves, the best m-term approximation $\tilde{f}_m$ by curvelet thresholding obeys the inequality $\|f - \tilde{f}_m\|_2^2 \leq C m^{-2} (\log m)^3$, while for wavelets the decay rate is only m^{-1}. Surprising performance has been shown in fields of image processing, see e.g. [10, 11, 12, 13, 14]. Recently, the 3D curvelet transform was presented by Ying *et al.* [9,8]. Unlike the isotropic elements of wavelets, the needle-shaped elements of this transform possess very high directional sensitivity and anisotropy (see Fig. 1 for 2D case). Such an element is very efficient for representing vortex edges of geophysical fluids images.

In a previous work [4], 2D curvelet transforms have been applied to the detection and tracking of some characteristic deformable structures of geophysical fluid in sea surface temperature satellite image sequences (from NOAA Advanced Very High Resolution Radiometerimage). However such detection do not take into account temporal consistency between successive frames. In this paper, we apply a 3D curvelet transform to fluid flow image sequences in or-

der to extract the evolution of spatio-temporal structures. Then a new curvelet reconstruction by combining the 3D curvelet transform with total variation minimization [18,13,14] is presented to further suppress the artifacts resulting from classical thresholding.

The paper is organized as follow : part II is devoted to the description of 3D curvelet transform and some classical threshold operations; part III describes the TV minimization technique and its combination with 3D curvelet transform: this forms the original part of this paper. Some numerical experiments showing applications of the later method to geophysical fluid flow image sequences are presented in part IV.

2 3D curvelet transform and thresholding

2.1 2D curvelet transform

In 1999, an anisotropic geometric wavelet called *ridgelet* was proposed by E. Candès and D. Donoho [5]. It is optimal at representing straight-line singularities. However its application is limited to objects with global straight-line singularities. In order to take into account images with local line or curve singularities, the so-called first generation of *Curvelet transform* [6] was developed using ridgelet transforms applied on sub-partitions of the image. A second generation of curvelet transform based on a frequency partition technique was introduced by the same authors in 2004 [7]. A 2D discrete curvelet transform was implemented in 2004 [8]: it is freely available at `http://www.curvelet.org`.

The 2D continuous curvelet transform can be defined as follow. Let W : $[1/2, 2] \mapsto \mathbb{R}$ and V : $[-1, 1] \mapsto \mathbb{R}$ be respectively a *radial* and an *angular* windows – in the spatial domain –, supported on $[1/2, 2]$ and $[-1, 1]$ respectively and obeying the admissibility condition

$$\sum_{l=-\infty}^{-\infty} V^2(t-l) = 1, \quad t \in \mathbb{R}, \tag{1}$$

$$\sum_{l=-\infty}^{-\infty} W^2(2^{-j}r) = 1, \quad r > 0. \tag{2}$$

For instance, the following Meyer windows [13] satisfy the above conditions:

$$V(t) = \begin{cases} 1 & |t| \leq 1/3, \\ \cos[\frac{\pi}{2}\nu(3|t|-1)] & 1/3 \leq |t| \leq 2/3, \\ 0 & \text{else.} \end{cases} \tag{3}$$

$$W(r) = \min\left\{\cos(\frac{\pi}{2}\nu(5-6r)), \cos(\frac{\pi}{2}\nu(3r-4))\right\} \tag{4}$$

where ν is a smooth function satisfying for all $x \in \mathbb{R}$:

$$\nu(x) = \begin{cases} 0 & x \leq 0, \\ 1 & x \geq 1, \end{cases} \quad \text{and} \quad \nu(x) + \nu(1-x) = 1. \tag{5}$$

$$\nu(x) = \begin{cases} 0 & x \leq 0, \\ \frac{1}{2}(\sin[\frac{\pi}{2}(2x-1)]+1) & x \leq 1, \\ 1 & \text{else.} \end{cases} \tag{6}$$
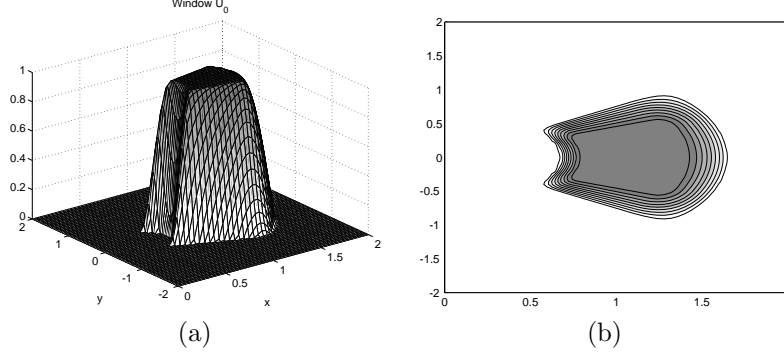
Figure 4: Frequency domain window U_0 (a) and its support (b).

As in wavelet theory, we also introduce a low-pass window W_{j_0}, $j_0 \geq 0$ which satisfies : for all $r \in \mathbb{R}$

$$W_{j_0}(r)^2 + \sum_{j > j_0} W^2(2^{-j}r) = 1. \tag{7}$$

Finally, let us denote by $\hat{f}$ the Fourier transform of an element f of $L^2(\mathbb{R})$: it is a function of the frequency variables $\xi = (\xi_1, \xi_2)$ with polar coordinates (r, θ).

Curvelets are indexed by three integers j, k and l which respectively stand for *scale*, *location* and *orientation*.

Curvelets at the coarsest scale $j = j_0$ are defined through their Fourier transform by

$$\varphi_{j_0,0,k}(x) = \varphi_{j_0}(x - 2^{-j_0}k), \quad k = \mathbb{Z}^2, \tag{8}$$

where

$$\hat{\varphi}_{j_0}(\xi) = 2^{-j_0}W_{j_0}(2^{-j_0}|\xi|). \tag{9}$$

At this scale, curvelets are then isotropic.

Curvelets at the finest scales. For each scale $j > j_0$, we define a window U_j in the frequency domain for all $\xi = (\xi_1, \xi_2)$ with polar coordinates (r, θ) by

$$U_j(\xi) = 2^{-3j/4}W(2^{-j}r)V\left(\frac{2^{\lfloor j/2 \rfloor}\theta}{2\pi}\right), \tag{10}$$

where $\lfloor \cdot \rfloor$ denotes the integer part operator. The support of U_j is a polar 'wedge' determined by $\text{supp}(r \mapsto W(2^{-j}r)) = [2^{j-1}, 2^{j+1}]$ and $\text{supp}(\theta \mapsto V(2^{\lfloor j/2 \rfloor}\theta)) = [-2^{-\lfloor j/2 \rfloor}, 2^{-\lfloor j/2 \rfloor}]$. Figure 4 shows the first window U_0 in the frequency domain when the radial and angular windows are defined by (3) and (4) respectively and when ν given by (6) [12]. We consider a uniform discretisation of the angle coordinate $\theta \in [0, 2\pi[$

$$\theta_l = 2\pi \times l \times 2^{-\lfloor j/2 \rfloor}, \quad 0 \leq l < 2^{\lfloor j/2 \rfloor}, \tag{11}$$

and the rotation by θ radians matrix

$$R_\theta = \begin{pmatrix} \cos\theta & \sin\theta \\ -\sin\theta & \cos\theta \end{pmatrix}. \tag{12}$$
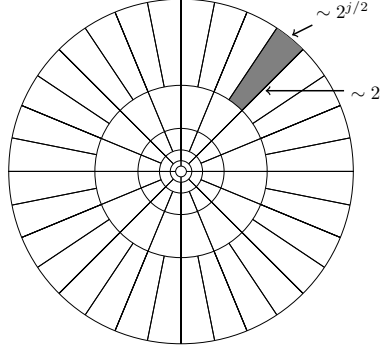
Figure 5: Frequency plane partition. The shaded area shows an example of a "wedge" on which a curvelet is supported in the frequency plane. At scale j, this wedge has a width of order 2^j and a length of order $2^{j/2}$.

Note that the number of discrete orientations θ_l depends on the scale index j : this number is doubled when scale change from an odd index $2j + 1$ to the larger next even one $2j + 2$. It is unchanged when scale index is changing from $2j$ to $2j + 1$ (see Fig. 5). At the finest scales $j > j_0$, curvelets are defined for all $x \in \mathbb{R}^2$ by

$$\varphi_{j,k,l}(x) = \varphi_j \left(R_\theta(x - x_k^{(j,l)}) \right) \tag{13}$$

where the waveform φ_j is the inverse Fourier transform of the frequency window U_j and the translation vector $x_k^{(j,l)}$, $k = (k_1, k_2) \in \mathbb{Z}^2$ is defined by

$$x_k^{(j,l)} = R_{\theta_l}^{-1}(2^{-j}k_1, 2^{-j/2}k_2). \tag{14}$$

It can be proved [7] that the above family of curvelets defines a *tight frame* (see [28] for a detailed definition of this term): for all $f \in L^2(\mathbb{R}^2)$ we have (Parseval equality)

$$\sum_{j,k,l} |\langle f, \varphi_{j,k,l} \rangle|^2 = \|f\|_{L^2(\mathbb{R}^2)}^2, \tag{15}$$

and the reconstruction formula

$$f = \sum_{j,k,l} \langle \varphi_{j,k,l}, f \rangle \varphi_{j,k,l}, \tag{16}$$

where $\langle \cdot, \cdot \rangle$ is the usual inner product in $L^2(\mathbb{R}^2)$: $\langle f, g \rangle = \int_{\mathbb{R}^2} \bar{f} g$.
Remarks:

- Curvelet coefficients in (16) are determined by

$$c_{j,k,l} := \langle \varphi_{j,k,l}, f \rangle = \frac{1}{(2\pi)^2} \int \hat{f}(\xi) \overline{U_j(R_{\theta_l}\xi)} e^{i \langle x_k^{(j,l)}, \xi \rangle} d\xi \tag{17}$$

- In practice we use Discrete Curvelet Transform (DCT) which is designed for f defined on a Cartesian grid $\{(n_1, n_2) \in \mathbb{N}, \quad 0 \le n_1, n_2 < n \in \mathbb{N}\}$. Digital coefficients are defined

$$c_{j,k,l}^D = \sum_{n_1,n_2} f(n_1, n_2) \overline{\varphi_{j,k,l}^D(n_1, n_2)} \tag{18}$$

where the construction of the digital curvelet waveforms φ^D is an adaptation of the above continuous transform for Cartesian grids. This lead to a non uniform discretisation of the orientations. For more details and C++ implementation see below and [8].

2.2   3D curvelet transform

The 3D curvelet transform was proposed by Ying *et al.* [9]. A fast application of the 3D curvelet transform to 3D turbulent flows has been presented by Ma *et al.* [15]. The so-called second-generation curvelet discrete transform used in this paper is based on a frequency partition technique. Similar to 2D problems, we define $V(t)$ and $W(r)$ to be a pair of smooth, non-negative real-valued window functions, which are called angular window and radial window, respectively. V is supported on $[-1, 1]$ and W on $[\frac{1}{2}, 2]$. The windows should satisfy admissibility conditions described in [8]. Without loss of generality, we introduce the lowpass window W_0 for the coarsest scale, which satisfies the condition

$$W_0(r)^2 + \sum_{j>0} W(2^{-j}r)^2 = 1. \tag{19}$$

For example, these conditions are satisfied by taking the scaled Meyer windows (3) and (4) [13]. For each $j > 0$, the radial window $W(2^{-j}r)$ smoothly extracts the frequency content inside the dyadic corona $2^{j-1} \leq r \leq 2^{j+1}$. The angular windows partition of $\mathbb{R}^3$ into trapezoidal regions obeying frequency parabolic scaling (thickness $\approx$ lengh^2) [9]. For $j \geq 0$, define the window $U_j(\xi)$, $\xi = (\xi_1, \xi_2, \xi_3) \in \mathbb{R}^3$ in frequency domain as

$$U_j(\xi) = 2^{-3j/4} W(2^{-j}|\xi|) V(2^{\lfloor j/2 \rfloor}\theta), \qquad \xi \in \mathbb{R}^3, \tag{20}$$

where $(|\xi|, \theta)$ denotes the polar coordinates corresponding to ξ. The support of U_j is a 3D polar wedge shape, i.e., a half circular cone (see Fig. 3 in [9]).

The system of curvelets is now indexed by three parameters (j, l, k) where j denotes scale, l denotes orientation, and $k = (k_1, k_2, k_3)$ denotes spatial location. Define the curvelets as

$$\varphi_{j,l,k}(x) := \varphi_j(R_{\theta_{j,l}}(x - x_k^{(j,l)})), \qquad x = (x_1, x_2, x_3) \in \mathbb{R}^3 \tag{21}$$

where $\widehat{\varphi}_j(\xi) := U_j(\xi)$, i.e., U_j is the Fourier transform of φ_j, $R_{\theta_{j,l}}$ denotes the rotation matrix with angle $\theta_{j,l}$. Figure 6 shows an element of 3D curvelets. Observe that in the spatial domain, $\varphi_{j,l,k}$ is of plate-like shape, which rapidly decays away from a 2^{-j} by $2^{-j/2}$ cross-section rectangle with center $x_k^{(j,l)}$ and orientation $\theta_{j,l}$ with respect to the vertical axis in x. The element is smooth within the plate but exhibits oscillating decay in the normal direction of the plate. It obeys a parabolic scaling law between the thickness and length (thickness $\approx$ lengh^2) and directional sensitivity (Orientations $= 1/\sqrt{\text{scale}}$).

Let $\mu = (j, l, k)$ be the collection of the triple index again. The curvelet coefficients are given by

$$\begin{aligned} c_\mu(f) : &= \langle f, \varphi_\mu \rangle = \int_{\mathbb{R}^3} \hat{f}(\xi) \overline{\widehat{\varphi}_\mu(\xi)} d\xi \\ &= \int_{\mathbb{R}^3} \hat{f}(\xi) \overline{U_j(R_{\theta_{j,l}}\xi)} e^{i\langle x_k^{(j,l)}, \xi \rangle} d\xi. \end{aligned} \tag{22}$$
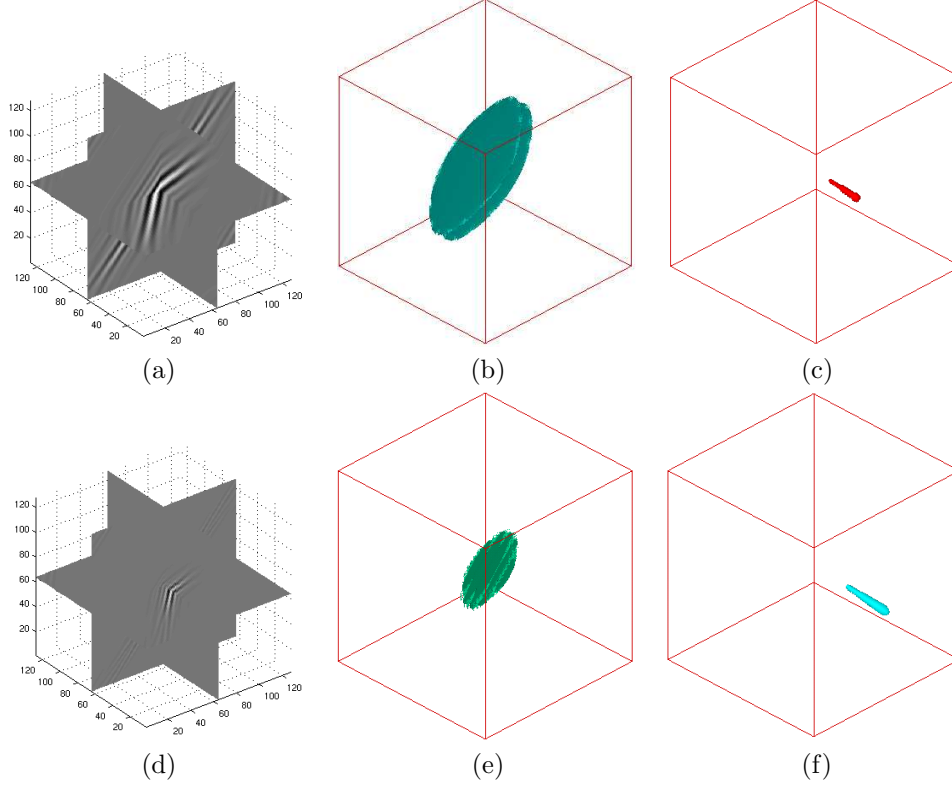
Figure 6: An element of 3D curvelets at a coarse scale (upper row) and fine scale (lower row) is shown in three cross-sections (left column) and isosurface (middle column). The right column shows their frequency support. It can be clearly seen that the element with high resolution in the space domain has low resolution ion in the frequency domain. But the supports in space and frequency domain are both local.

In order to have Cartesian coronae, which is based on concentric cubes instead of sphere, the authors of [9, 8] applied a pseudo-polar grid by a modified window of the form

$$\widetilde{W}_0(\xi) = \Phi_0(\xi), \ \widetilde{W}_j(\xi) = \sqrt{\Phi_{j+1}^2(\xi) - \Phi_j^2(\xi)}, \ j > 0, \tag{23}$$

where $\Phi_j(\xi_1, \xi_2, \xi_3) = \phi(2^{-j}\xi_1) \cdot \phi(2^{-j}\xi_2) \cdot \phi(2^{-j}\xi_3)$, the one-dimensional window ϕ satisfying $0 \leq \phi \leq 1$, $\operatorname{supp}\phi \subset [-2, 2]$ and $\phi(r) = 1$ for $r \in [-1/2, 1/2]$. As before, ϕ can be taken to be a scaled Meyer window. The angular window for the l-th wedge can be redefined as

$$\widetilde{V}_{j,l}(\xi) = V\left(2^{j/2} \cdot \frac{\xi_2 - \alpha_l \cdot \xi_1}{\xi_1}\right) \cdot V\left(2^{j/2} \cdot \frac{\xi_3 - \beta_l \cdot \xi_1}{\xi_1}\right). \tag{24}$$

Here $(1, \alpha_l, \beta_l)$ is the direction of the centre line of the wedge. Every Cartesian corona has six components. The windows in the other five components have similar definitions.

Now we define the modified frequency window $\widetilde{U}$ as

$$\widetilde{U}_{0,0}(\xi) = \widetilde{W}_0(\xi), \ j = 0, \tag{25}$$

$$\widetilde{U}_{j,l}(\xi) = \widetilde{W}_j(\xi) \cdot \widetilde{V}_{j,l}(\xi), \ 0 < j < j_f, \tag{26}$$

and at the finest scale j_f, the wavelet-like isotropic element is defined by the frequency window $\widetilde{U}_{j_f,0}(\xi) = \widetilde{W}_{j_f}(\xi)$. It is clear that $\widetilde{U}_{j,l}$ $(0 < j < j_f)$ isolates frequencies near the wedge

$$(\xi_1,\xi_2,\xi_3): 2^{j-1} \le \xi_1 \le 2^{j+1}, \ -2^{-j/2} \le \xi_2/\xi_1 - \alpha_l \le 2^{-j/2}, \ -2^{-j/2} \le \xi_3/\xi_1 - \beta_l \le 2^{-j/2}. \tag{27}$$

Let $L_{p,j,l}$ $(p = 1, 2, 3)$ be three positive integers satisfying

  (i) One can not find ξ and ξ' such that $\xi_p - \xi'_p$ are multiples of $L_{p,j,l}$;

  (ii) The volume $\Lambda_{j,l} = L_{1,j,l} \cdot L_{2,j,l} \cdot L_{3,j,l}$ is minimal.

The two previous conditions guarantee that the data does not overlap with itself during the wrapping process below. Obviously, the $\widetilde{U}_{j,l}$ is supported now in a 3D rectangular box of integer size $L_{1,j,l} \times L_{2,j,l} \times L_{3,j,l}$.

The discrete curvelets are given by their Fourier formation

$$\hat{\varphi}_\mu^D(\xi) = \widetilde{U}_{j,l}(\xi) \cdot \exp\left(-2\pi i \sum_{p=1,2,3} \frac{k_p \xi_p}{L_{p,j,l}}\right) / \sqrt{\Lambda_{j,l}} \tag{28}$$

for $0 < k_p < L_{p,j,l}$, $p = 1, 2, 3$.

Analogously, the transform at the coarsest level is defined as

$$\hat{\varphi}_{0,0,k}^D(\xi) = \widetilde{U}_{0,0}(\xi) \cdot \exp\left(-2\pi i \sum_{p=1,2,3} \frac{k_p \xi_p}{L_{p,0}}\right) / \sqrt{\Lambda_0}, \tag{29}$$

and a similar formula can be obtained at the finest scale by replacing the scale 0 with j_f and setting $L_{p,j_f} = n$.

Now we can find the Cartesian counterpart of the coefficients in (22) by

$$\tilde{c}_\mu^D(f) = \langle f, \varphi_\mu^D \rangle = \int_{\mathbb{R}^3} \mathcal{W}(\widetilde{U}_{j,l}(\xi)\hat{f}(\xi)) \, e^{i\langle k_j, \xi \rangle} d\xi. \tag{30}$$

The algorithm of three-dimensional discrete curvelet transform is summarized as follow:

  1. Apply the 3D FFT and obtain Fourier samples $\hat{f}(\xi)$, $-n/2 \le \xi < n/2$, $\xi = (\xi_1, \xi_2, \xi_3)$.
  2. Multiply the frequency window $\widetilde{U}_{j,l}(\xi) \hat{f}(\xi)$ for each scale j and angle l.
  3. Wrap around the origin and obtain $\mathcal{W}(\widetilde{U}_{j,l}f)(\xi)$, where the range for ξ_p is $-L_{p,j,l}/2 \le \xi_p < L_{1,j,l}/2$, $j = (0, j_f)$. No wrapping at scales 0 and j_f.
  4. Apply 3D inverse FFT to each $\mathcal{W}(\widetilde{U}_{j,l}f)$ to obtain the discrete coefficients c_μ^D.

The computational complexity of the DCuT is $O(n^3 \log n)$ flops for $n \times n \times n$ data [8].

Reconstruction of threshold-processed curvelet coefficients

$$u_c = \sum_\mu \tau(\tilde{c}_\mu^D(f))\, \varphi_\mu, \tag{31}$$

leads to denoising or extraction of videos. Here $\tau(x)$ denotes a thresholding function. Some classical thresholding functions are listed below [16]:

1) Hard thresholding

$$\tau(x) = \begin{cases} x, & |x| \geq \sigma, \\ 0, & |x| < \sigma, \end{cases} \tag{32}$$

2) Soft thresholding

$$\tau(x) = \begin{cases} x - \sigma, & x \geq \sigma, \\ 0, & |x| < \sigma, \\ x + \sigma & x \leq -\sigma, \end{cases} \tag{33}$$

3) Firm thresholding

$$\tau(x) := \begin{cases} x - \frac{\sigma^2}{x}, & |x| \geq \sigma, \\ 0, & |x| < \sigma, \end{cases} \tag{34}$$

4) SCAD by Antoniadis and Fan [17]

$$\tau(x) = \begin{cases} sign(x)\max(0, |x| - \sigma), & |x| \leq 2\sigma, \\ \frac{(\alpha - 1)x - \alpha\sigma sign(x)}{\alpha - 2}, & 2\sigma < |x| < \alpha\sigma, \\ x, & |x| \geq \alpha\sigma. \end{cases} \tag{35}$$

Generally, we choose $\alpha = 3.7$. Here σ is a given threshold value.

3 TV-SYNTHESIS 3D CURVELET SHRINK-AGE

It has been well known that tools from computational harmonic analysis suffer from pseudo-Gibbs phenomena (i.e., oscillation artifacts near the discontinuities), although curvelets have much improved the problem in comparison to traditional wavelets. Reconstructing the coefficient using a rule of total variation (TV) minimisation can reduce the pseudo-Gibbs and element-like artifacts [18, 13, 14].

Following the previous work, here we combine the TV technique with 3D curvelet transform for the first time. The TV-synthesis curvelet shrinkage can reduce the artifacts and sharpen the blurry edges in extracted fields.

For a function u with $|\nabla u| \in L^1(\Omega)$, the total variation functional is defined by [19]

$$TV(u) = \int_\Omega |\nabla u(x)|\, dx. \tag{36}$$

In order to avoid computational difficulties arising from the non-differentiation of the modulus at zero, the TV functional is often replaced by

$$TV(u) = \int_\Omega \sqrt{|\nabla u(x)|^2 + \beta^2}\, dx, \tag{37}$$

where $\beta > 0$ is a small parameter. In the following description, we mainly restrict our attention to the 3D problem. For the 2D problem, we refer readers to [12, 13], where the authors have combined TV minimisation with the ridgelet and curvelet transform for image processing. Using a first order finite differences scheme for computing the gradient, the total variation functional for $u := (u_{\iota,\kappa,\nu},)_{(\iota,\kappa,\nu)\in\mathbb{I}_n^3}$ is given by

$$TV(u) = \sum_{\iota,\kappa,\nu} \sqrt{(\delta_1 u)_{\iota,\kappa,\nu}^2 + (\delta_2 u)_{\iota,\kappa,\nu}^2 + (\delta_3 u)_{\iota,\kappa,\nu}^2 + \beta^2}\, dx, \qquad (38)$$

where $(\delta_1 u)_{\iota,\kappa,\nu} = u_{\iota+1,\kappa,\nu} - u_{\iota,\kappa,\nu}$, $(\delta_2 u)_{\iota,\kappa,\nu} = u_{\iota,\kappa+1,\nu} - u_{\iota,\kappa,\nu}$, and $(\delta_3 u)_{\iota,\kappa,\nu} = u_{\iota,\kappa,\nu+1} - u_{\iota,\kappa,\nu}$. More precisely, for a given u let

$$\mathbb{U} := \{u := (u_{\iota,\kappa,\nu})_{(\iota,\kappa,\nu)\in\mathbb{I}_n^3} : c_{\mu>}^D = c_\mu^D, \forall \mu \in \Lambda\}. \qquad (39)$$

Then we are looking for the solution of the constrained minimisation problem

$$\min_{u\in\mathbb{U}} TV(u). \qquad (40)$$

If the linear subspace $\mathbb{V}$ consists of functions on $\mathbb{I}_n^3$ given by

$$\mathbb{V} := \{v := (v_{\iota,\kappa,\nu})_{(\iota,\kappa,\nu)\in I_n^3} : c_\mu^D = 0, \forall \mu \in \Lambda\}, \qquad (41)$$

the idea of TV-minimisation is to remove the pseudo-Gibbs oscillations by minimizing the functional

$$F(u) = \int_\Omega |u - u_0|^2\, dx + \lambda\, TV(u) \qquad (42)$$

for $u \in \{u_c + v, v \in \mathbb{V}\}$, where u_0 is an original flow, u_c is a reconstructed flow after curvelet hard thresholding, and $\mathbb{V}$ is a linear subspace of functions consisting of the components removed by thresholding. It should be noted that because of the constraint on the subspace $\mathbb{V}$, Eq. (42) is not the usual Rudin-Osher-Fatemi's TV model as in Ref. [19], but instead is a variant of the TV problem, which was originally inspired by Durand *et al.* [18] for wavelets and extended by Ma *et al.* [14, 13, 12].

Using u_c as an initial guess, the constrained TV-minimisation can be computed by a projected subgradient descent scheme [18]

$$u^{l+1} = u^l - t_l\, P_V(g_{TV}(u^l)). \qquad (43)$$

Here $g_{TV}(u)$ denotes the subgradient of TV at u. The step size t_l can be taken appropriately to ensure convergence. $P_V(u)$ denotes a projection of u on the constrained subspace $\mathbb{V}$. This means that only the coefficients with absolute value smaller than a given threshold σ will be changed by the minimisation process. Let T be the curvelet transform and T^{-1} be its inverse, then we have $P_V(u) = T^{-1}\tau^{-1} T(u)$ where τ^{-1} denotes the so-called inverse thresholding function,

$$\tau^{-1}(x) := \begin{cases} 0, & |x| \geq \sigma \\ x, & |x| < \sigma. \end{cases} \qquad (44)$$

A crucial step is to compute the gradient of total variation, i.e., $g_{TV}(u)$ or $\nabla_u TV(u)$.
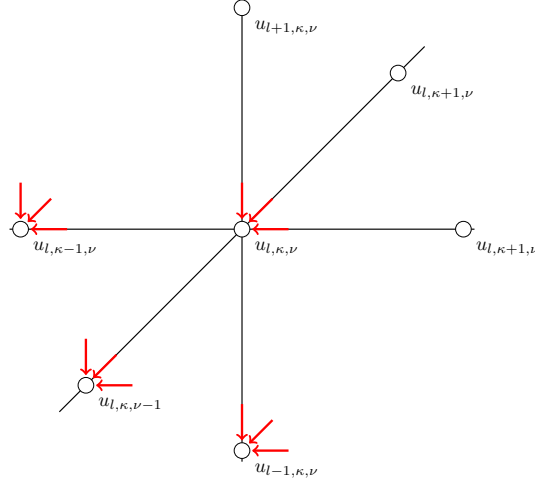
Figure 7: Diagram of 3D coordinate grid for computation of $\nabla_u TV(u)$. The four points with red arrow are points related to the derivation of the sum with respect to $u_{\iota,\kappa,\nu}$. The arrow head indicates the Euler forward difference scheme.

Figure 7 illustrates the 3D grids for computation of $\nabla_u TV(u)$ for 3D problems. The four points denoted by red arrow are points that are related to the derivation of the sum with respect to $u_{\iota,\kappa,\nu}$. The arrow head indicates the direction of the Euler forward difference scheme. The derivation of the total variation at location $u_{\iota,\kappa,\nu}$ is given by

$$
\begin{aligned}
\nabla_u TV(u) : \quad = \quad & (3u_{\iota,\kappa,\nu} - u_{\iota+1,\kappa,\nu} - u_{\iota,\kappa,\nu+1} - u_{\iota,\kappa+1,\nu}) \cdot A^{-1/2} \\
& + (u_{\iota,\kappa,\nu} - u_{\iota,\kappa-1,\nu}) \cdot B^{-1/2} \\
& + (u_{\iota,\kappa,\nu} - u_{\iota,\kappa,\nu-1}) \cdot C^{-1/2} \\
& + (u_{\iota,\kappa,\nu} - u_{\iota-1,\kappa,\nu}) \cdot D^{-1/2}
\end{aligned} \tag{45}
$$

for the inner points $(\iota,\kappa) \in \mathbb{I}_n^3$ and corresponding modification at the boundary $\partial \mathbb{I}_n^3$. Here

$$
A = (u_{\iota+1,\kappa,\nu} - u_{\iota,\kappa,\nu})^2 + (u_{\iota,\kappa,\nu+1} - u_{\iota,\kappa,\nu})^2 + (u_{\iota,\kappa+1,\nu} - u_{\iota,\kappa,\nu})^2, \tag{46}
$$

$$
B = (u_{\iota+1,\kappa-1,\nu} - u_{\iota,\kappa-1,\nu})^2 + (u_{\iota,\kappa-1,\nu+1} - u_{\iota,\kappa-1,\nu})^2 + (u_{\iota,\kappa,\nu} - u_{\iota,\kappa-1,\nu})^2, \tag{47}
$$

$$
C = (u_{\iota+1,\kappa,\nu-1} - u_{\iota,\kappa,\nu-1})^2 + (u_{\iota,\kappa+1,\nu-1} - u_{\iota,\kappa,\nu-1})^2 + (u_{\iota,\kappa,\nu} - u_{\iota,\kappa,\nu-1})^2, \tag{48}
$$

$$
D = (u_{\iota,\kappa,\nu} - u_{\iota-1,\kappa,\nu})^2 + (u_{\iota-1,\kappa,\nu+1} - u_{\iota-1,\kappa,\nu})^2 + (u_{\iota-1,\kappa+1,\nu} - u_{\iota-1,\kappa,\nu})^2. \tag{49}
$$

Essentially, TV minimisation does not set the insignificant coefficients to zero as conventional shrinkage does, but typically removes optimally small values to eliminate the artifacts. This 3D TV constrain method can be also incorporated easily into other transforms such as wavelets, contourlets and Surfacelets [21].

4 Numerical experiments

In this section, we will assess abilities of the 3D curvelet transform combined with TV-minimisation based thresholding for denoising and extracting from image sequences some pertinent structures of the observed geophysical fluids.

4.1 Simulated fluid motion video data (denoising and edge extraction)

Fig. 8 (a) shows a 3D vortex video of a simulated geophysical flows with 128 frames. It shows the motion of a vortex in a fluid submitted to the Coriolis force. Image pixels correspond to the concentration of a passive tracer which is advected by the velocity field (computed by the model). Fig. 8 (b) shows the result of using reconstruction of detailed coefficients of 3D wavelet transform [20]. Fig. 8 (c) is obtained using the 3D curvelet transform described in section 2. Both transforms can capture the edges. However, curvelet transform results to be smoother and more continues along the edges than wavelet transform does. It can be seen obviously that oscillating artifacts arise along the edges with wavelet transform: it is due to its poor abilities for representing curve-line singularities. It is also possible to extract edge structures in noisy environment. Fig. 9 shows 3D evolution of a flow with Gaussian white noise. Fig. 9 (b) and (c) show the denoising results by 3D wavelet transform and curvelet transform, respectively. Fig. 9 (d) and (e) are the edge mapping of (b) and (c) using simple reconstruction of detailed coefficients after hard thresholding. The 3D curvelet shows its good performances for edge-preserving denoising and feature extraction.

In these above tests, we only use the simplest hard thresholding for wavelet and curvelet transform. Many advance techniques including contrast enhancement (e.g., [11]) can be incorporated into this framework. Now we will show the abilities of the proposed 3D TV-synthesis curvelet shrinkage. Figure 10 (a) shows part of the 3D vortex video with white noise. Fig. 10 (b) is the denoising result by curvelet transform. It should be noticed that analysing such kind of images with weak features using conventional methods is a challenging problem. Indeed the edges are too blurry and almost without high-frequency components. Using our TV-synthesis curvelet transform can sharpen the edges to some extent when we remove the noise: Fig. 10 (c). Fig. 10 (d) shows the removed components in our curvelet denoising. Some edge structures have been kicked out yet. There is a big room for future researches in image processing communities.

4.2 Real fluid motion video data (denoising and edge extraction)

Fig. 11 shows denoising result by wavelets and TV-synthesis curvelet transform of a real – then noisy – EUMETSAT (water vapour channel) video data showing the evolution of a vorticity band. Fig. 11 (a) is a frame of original flows with noisy. Fig. 11 (b) and (c) are the denoising result by 3D wavelet transform and its removed components, respectively. Fig. 11 (d) and (e) are results by 3D TV-synthesis curvelet denoising with 0.005 stepsize and 10 iterations, and its removed components. The SNR (signal-to-noise ratio) of wavelet and curvelet's

denoising results are 38.95 dB and 42.96 dB. In order to see clear the difference, Fig. 12 shows the close-up of the original flow, wavelet denoising result, and curvelet denoising result. It can be seen obviously that the results by our proposed method preserve the edges much better than those by wavelet method. The oscillating artifacts and element-like artifacts that appear in wavelet's results are almost suppressed by our TV-synthesis curvelet method. However, the orthogonal wavelet transform is much faster than the curvelet method. Specially for this case, the elapsed time of forward 3D wavelet transform is 0.54 seconds, and inverse transform is 0.45 seconds. The elapsed time of forward curvelet transform and inverse curvelet transform are 1.55 seconds and 1.65 seconds, while the TV-synthesis curvelet transform has to pay 85.0 seconds.

Fig. 13 shows edge extraction using wavelet transform, curvelet transform combined with hard thresholding and TV-synthesis curvelet transform. Fig. 14 displays the respective close-up amplification. The curvelet-based methods show good abilities to extract line-like geometric edges. These extracted spatio-temporal geometric structures will be used in our sequent work on image assimilation of geophysical fluids. This is also one of main motivations of this paper.

4.3 Video data containing high frequency edges and textures (denoising)

The proposed method can be widely used in other fields. Indeed, the TV-synthesis curvelet transform is more significant for images with high-frequency edges and textures. We give an example of real video data (the data was also used in [21]) to further show the outstanding performance of our method, in comparison to existing wavelet methods. Fig. 15 (a) shows the 3D noisy video consisting in line edges and point features. Fig. 15 (b) is the denoising result using 3D wavelet transform. Analogically, Fig. 15 (c) is the edge-preserving denoising result using our TV-synthesis curvelet transform. Fig. 16 displays the close-up of Fig. 15 (a) (b) and (c), respectively. The proposed method preserves the edges better and also achieve much higher signal-noise-ratio SNR = 36.99 than those by wavelet SNR = 34.92 dB.

Finally, we should notice that we do not pay attention to criticise the wavelets here but to point out the respective advantages of using wavelets and curvelets. Indeed, wavelets are better at representing point-like features while curvelets are optimal for curve-like edges and structural features. Orthogonal wavelet transform is very fast and rich achievements on wavelet algorithm in other disciplines can be applied in our field. For a 64^3 data, the wavelet forward and inverse transform takes 0.83 seconds and 0.54 seconds while curvelet transform takes 1.29 seconds and 1.27 seconds; For a 128^3 data the wavelet takes 2.29 and 2.17 seconds while curvelet takes 26.82 and 56.26 seconds for the forward and inverse transform. At the present time, a fast parallel algorithm of 3D curvelet transform can be available at www.curelet.org for large-scale computations. Normally, the performances of curvelets for larger scale images are better than smaller scale images: indeed more decomposed levels can be used in large size problems so that the elements of curvelets have more anisotropic directional selectivity. Combining curvelets with wavelets would be promising for general geophysical fluids and natural image sequences.

(a)

(b)

(c)
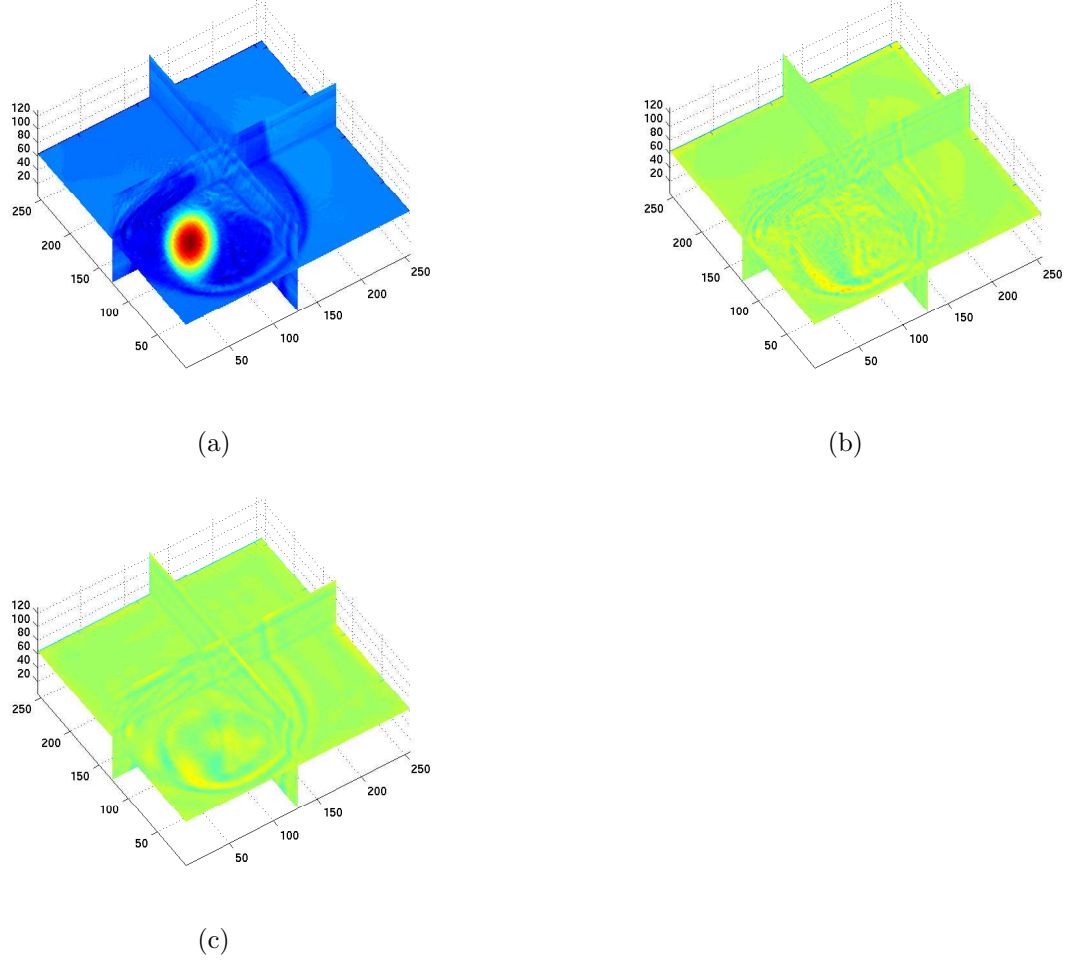
Figure 8: Extraction of edge structure. (a) original vortex flows. (b) extraction by 3D wavelets. (c) extraction by 3D curvelets.

5   Conclusion

In this paper, we investigated applications of 3D curvelet transform to extraction of spatio-temporal geometric structures from geophysical fluid flow image sequences and denoising. Extracting such structures and tracking their evolution is essential for future forecast systems. Indeed, new data assimilation techniques (namely Image Sequences Assimilation) which will take into account such spatio-temporal structured data are under development.

A total variation based 3D curvelet reconstruction is proposed in order to sharpen the edges and to suppress oscillating artifacts. It can be applied widely in other fields on image and video processing.

Acknowledgements

References

[1] F.-X. Le Dimet, O. Talagrand, Variational algorithms for analysis and assimilatoin of meteorological observations: theoretical aspects, Tellus, **38A**, 97-110 (1986).

[2] J. Blum, F.-X. Le Dimet, I. Navon, Data Assimilation for Geophysical Fuilds, Handbook of Numerical Analysis, Special Volume on Computational Methods for the Ocean and the Atmosphere (R. Temam and J. Tribbia, eds.), Elsevier, New York, pp. 1-63, (2008).

[3] I. Herlin, F. X. Le Dimet, E. Huot, J. P. Berroir, Coupling models and data: which possibilities for remotely-sensed images?, Chapter e-Environement: progress and challenges, pp. 365-383, Instituto Politecnico Nacional, Mexico, 2004.

[4] J. Ma, A. Antoniadis, F.-X. Le Dimet, Curvelet-based snake for multiscale detection and tracking of geophysical fluids, IEEE Trans. Geosci. Remote Sensing, **44** (12), 3626-3638 (2006).

[5] E. J. Candès, D. L. Donoho, Ridgelets: A key to higher-dimensional intermittency ?, R. Soc. Lond. Philos. Trans. Ser. A., **357**, 2495-2509 (1999)

[6] E. J. Candès, D. L. Donoho, Curvelets - a surprisingly effective nonadaptive representation for objects with edges, In Curves and Surface Fitting: Saint-Malo 1999, A. Cohen, C. Rabut, L. Schumaker (Eds.), Vanderbilt Univ. Press, Nashville, 2000, 105-120.

[7] E. J. Candès, D. L. Donoho, New tight frames of curvelets and optimal representations of objects with piecewise singularities, Comm. Pure Appl. Math., **57**, 219-266 (2004).

[8] E. J. Candès, L. Demanet, D. L. Donoho, L. Ying, Fast discrete curvelet transforms, Multiscale Model. Simul., **5** (3), 861-899 (2006).

[9] L. Ying, L. Demanet, E. Candès, 3D Discrete Curvelet Transform, Proc. of SPIE Wavelets XI, Vol. 5914, 591413, San Diego, CA, 2005.

[10] J. L. Starck, E. J. Candès, D. L. Donoho, The curvelet transform for image denoising, IEEE Trans. Image Process., **11**, 670-684 (2002).

[11] J. L. Starck, E. J. Candès, D. L. Donoho, Astronomical image representation by the curvelet transform, Astronomy and Astrophysics, **398**, 785-800 (2003).

[12] J. Ma, G. Plonka, Combined curvelet shrinkage and nonlinear anisotropic diffusion, IEEE Trans. Image Process., **16** (9), 2198-2206 (2007).

[13] J. Ma, Curvelets for surface characterization, Appl. Phys. Lett., **9**, 054109:1-3 (2007).

[14] J. Ma, M. Fenn, Combined complex ridgelet shrinkage and total variation minimization, SIAM J. Sci. Comput., **28** (3), 984-1000 (2006).

[15] J. Ma, M. Y. Hussaini, Three-dimensional curvelets for coherent vortex analysis of turbulence, Appl. Phys. Lett., **91**, 184101:1-3 (2007).

[16] A. Antoniadis, Wavelet methods in statistics: some recent developments an their applications, Statistics Surveys, **1**, 16-55 (2007).

[17] A. Antoniadis, J. Fan, Regularization of wavelets approximations, J. Amer. Statist. Assoc, **96** (455), 939-963 (2001).

[18] S. Durand, J. Froment, Reconstruction of wavelet coefficients using total variation minimization, SIAM J. Sci. Comput., **24**, 1754-1767 (2003).

[19] L. Rudin, S. Osher, E. Fatemi, Nonlinear total variation based noise removal algorithms, Physica D, **60** (1), 259-268 (1992).

[20] I. Daubechies, *Ten lectures on wavelets.* SIAM, Philadelphia, PA, 1992.

[21] Y. Lu, M. N. Do, Multidimensional Directional Filter Banks and Surfacelets, IEEE Trans. Image Process., **16** (4), 918-931 (2007).

[22] G. K. Korotaev, E. Huot, F.-X. Le Dimet, I. Herlin, S. V. Stanichnya, D. M. Solovyeva, L. Wu, Retrieving ocean surface current by 4-D variational assimilation of sea surface temperature images, Remote Sensing of Environment, **112**, 1464-1475 (2008).

[23] F.-X. Le Dimet, I. Souopgui, O. Titaud, A. Vidard, Assimilation of Images in Numerical Models in Geophysics, in *International Conference on Engineering Optimization EngOpt2008*, Rio de Jianeiro, Brazil, 01-05 June 2008.

[24] F.-X. Le Dimet, Anestis Antoniadis, Jianwei Ma, Isabelle Herlin, Etienne Huot, Jean-Paul Berroir, Assimilation of Images In Geophysical Models, in *International Science and Technology for Space*, Kanazawa, Japan, 2006.

[25] I. Herlin, E. Huot, J.-P. Berroir, F.-X. Le Dimet, G. Korotaev, Estimation of a motien field on satellite images from a simplified ocean circulation model, *ICIP International Conference on Image Processing*, 1077-1080, 2006

[26] B.K.P Horn and B.G. Schunck, Determining optical flow, AI, **17** (1-3), 185-203, 1981.

[27] Didier Auroux and Jérôme Fehrenbach, Identification of velocity fields for geophysical fluids from a sequence of images, submitted to *Int. J. Computer Vision*, 2008

[28] S. Mallat, *A Wavelet Tour of Signal Processing.* Academic Press, 1998.

[29] S. Mallat, W.L. Hwang, Singularity detection and processing with wavelets, IEEE Transa. Information Theory, **32** (2), 617-643 (1992).

[30] M. Farge, Wavelet transforms and their applications to turbulence Annual Review of Fluid Mechanics, **24**, 395-457 (1992).

[31] M. Farge, G. Pellegrino, K. Schneider, Coherent vortex extraction in 3D turbulent flows using orthogonal wavelets, Phys. Rev. Lett., **87** (5), 054501 (2001).

[32] A. Turiel, J. Isern-Fontanet, E. Garcia-Ladona, Wavelet filtering to extract coherent vortices from altimetric data, J. Atmospheric and Oceanic Tech., **24** (12), 2103-2119 (2007).

[33] J. Yano,M. Moncrieff, X. Wu, et al., Wavelet analysis of simulated tropical convective cloud systems. Part I: Basic analysis, J. Atmospheric Sci., **58** (8), 850-867 (2001).

[34] S. Chapa, V. Rao, G. Prasad, Application of wavelet transform to Meteosat-derived cold cloud index data over South America, Monthly Weather Review, **126** (9), 2466-2481 (1998).
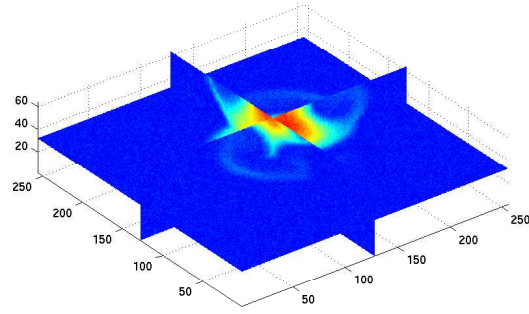
(a)
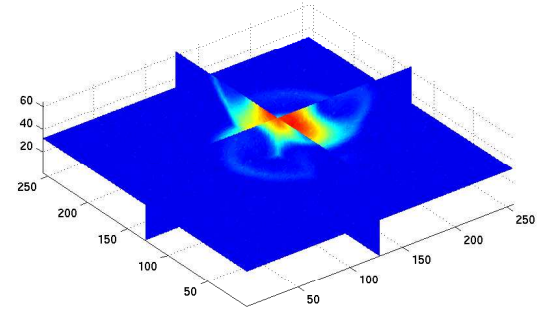
(b)
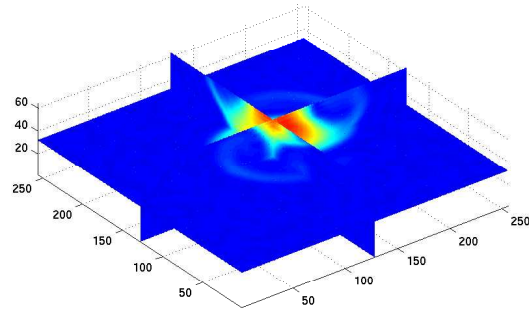
(c)
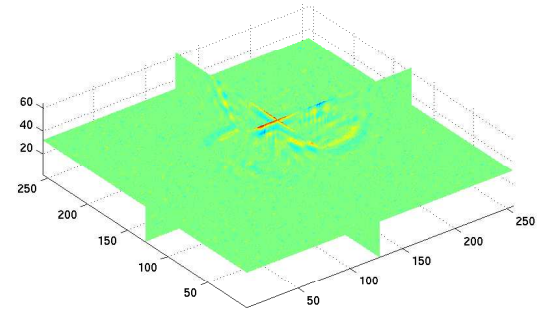
(d)
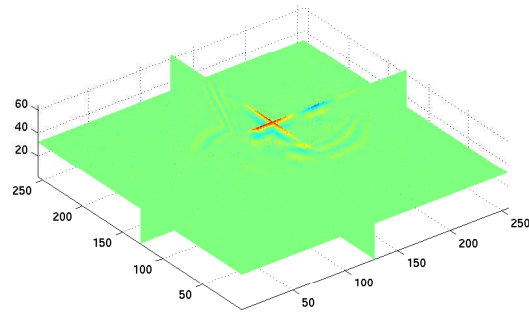
(e)

Figure 9: Extraction in noisy environment. (a) Noisy flows. (b) denoising by 3D wavelets. (c) denoising by 3D curvelets. (d) extraction by wavelets from (b). (e) extraction by curvelets from (c).
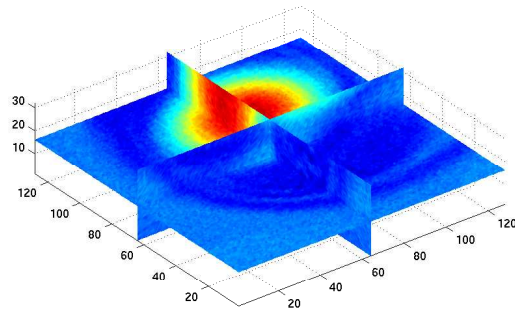
(a)
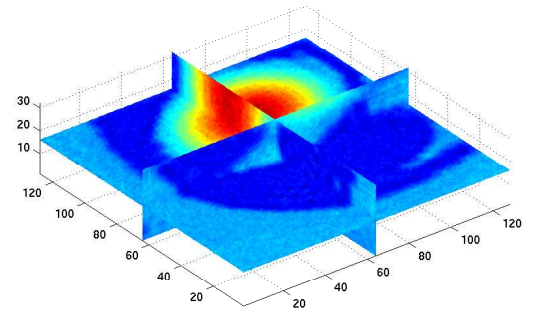
(b)
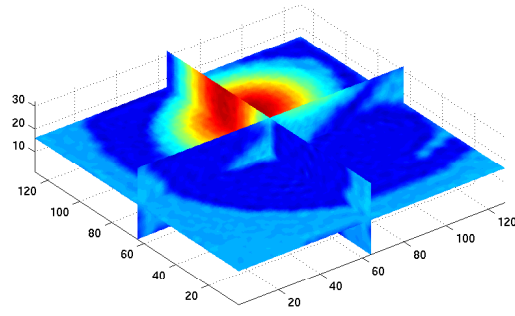
(c)
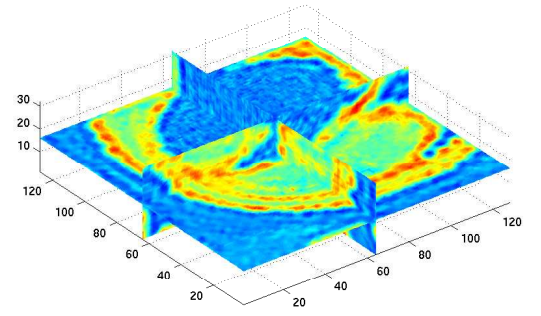
(d)

Figure 10: (a) Noisy flows. (b) denoising by the 3D curvelets. (c) denoising by the TV-synthesis curvelet transform. (d) removed components by (c).
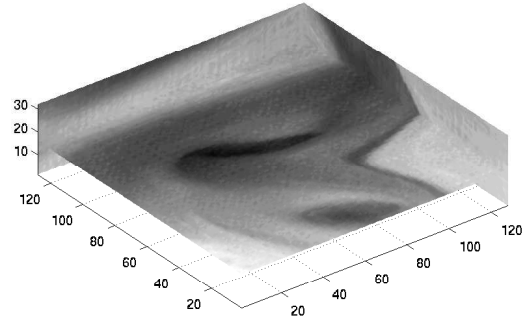
(a)
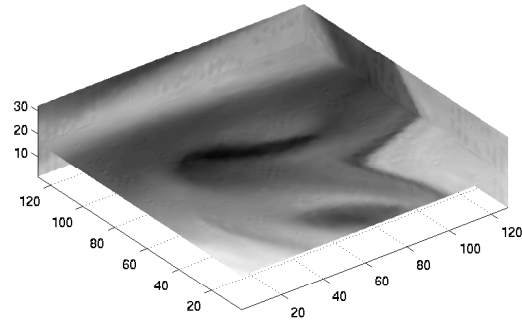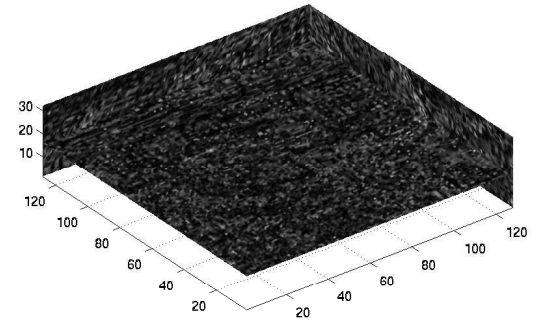
(b)   (c)
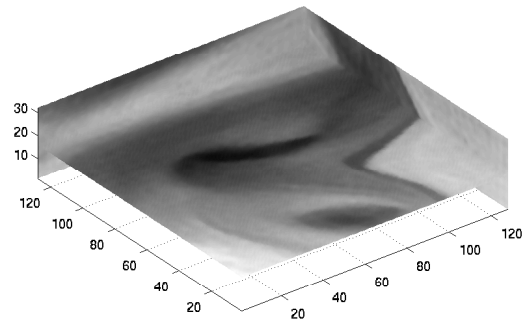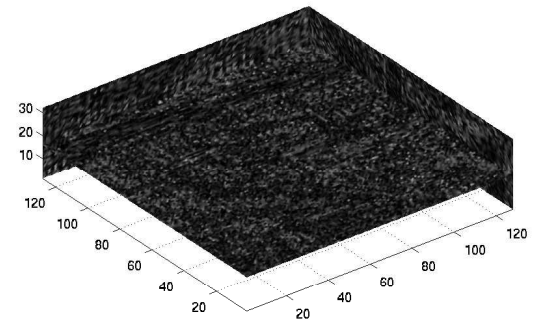
(d)   (e)

Figure 11: Denoising of an EUMETSAT real video data (water vapour channel) showing the evolution of a vorticity band . (a) the original noisy video. (b) and (c) 3D wavelet denoising (SNR = 38.95 dB) and its removed components. (d) and (e) 3D TV-synthesis curvelet denoising (SNR = 42.96 dB) and its removed components.

(a)
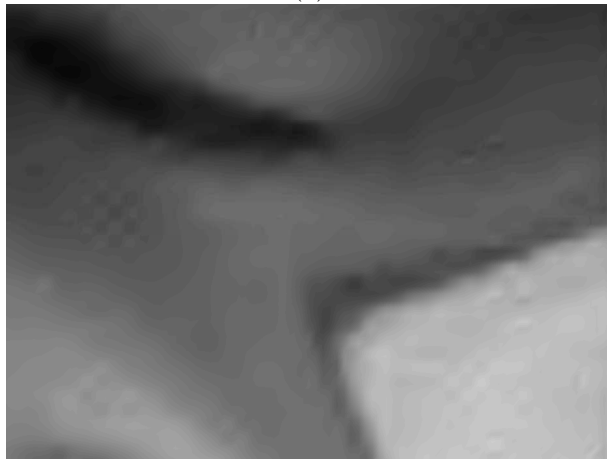
(b)
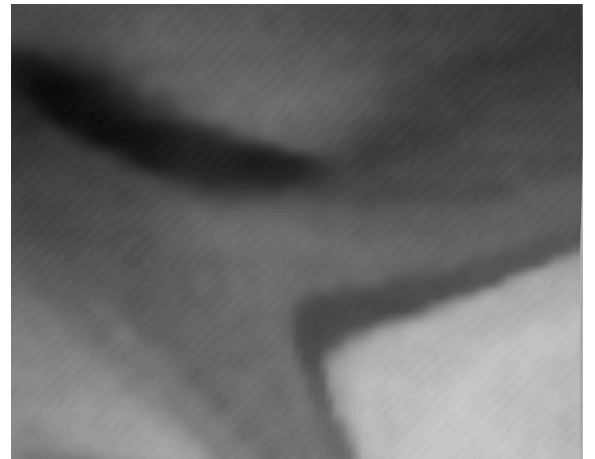
(c)

Figure 12: Close-up of Fig. 11. (a) Original noisy data. (b) wavelet denoising. (c) TV-synthesis curvelet denoising.
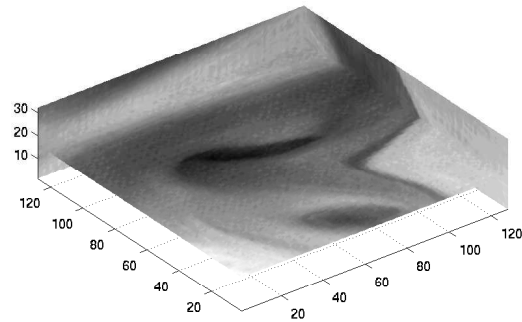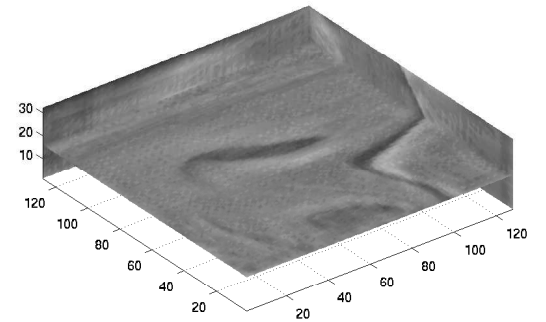
(a)   (b)
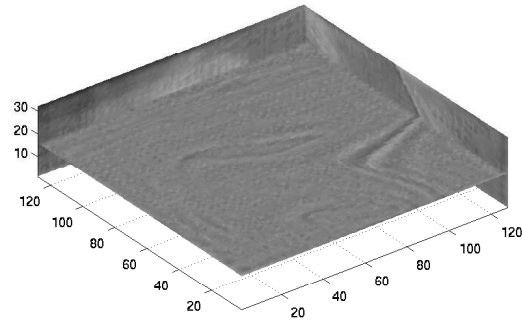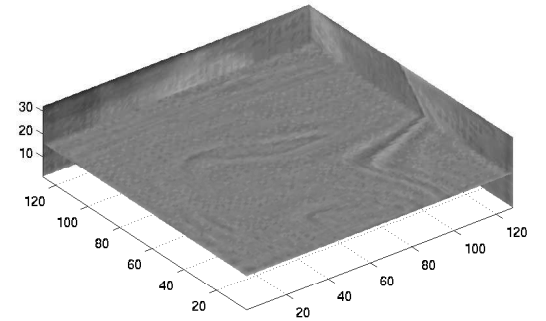
(c)   (d)

Figure 13: Edges extraction from a real noisy video data (EUMETSAT water vapour canal) showing the evolution of a vorticity band . (a) Original video. (b) Edges extraction with wavelets. (c) Edges extraction with curvelets. (d) Edges extraction by the TV-synthesis curvelet transform
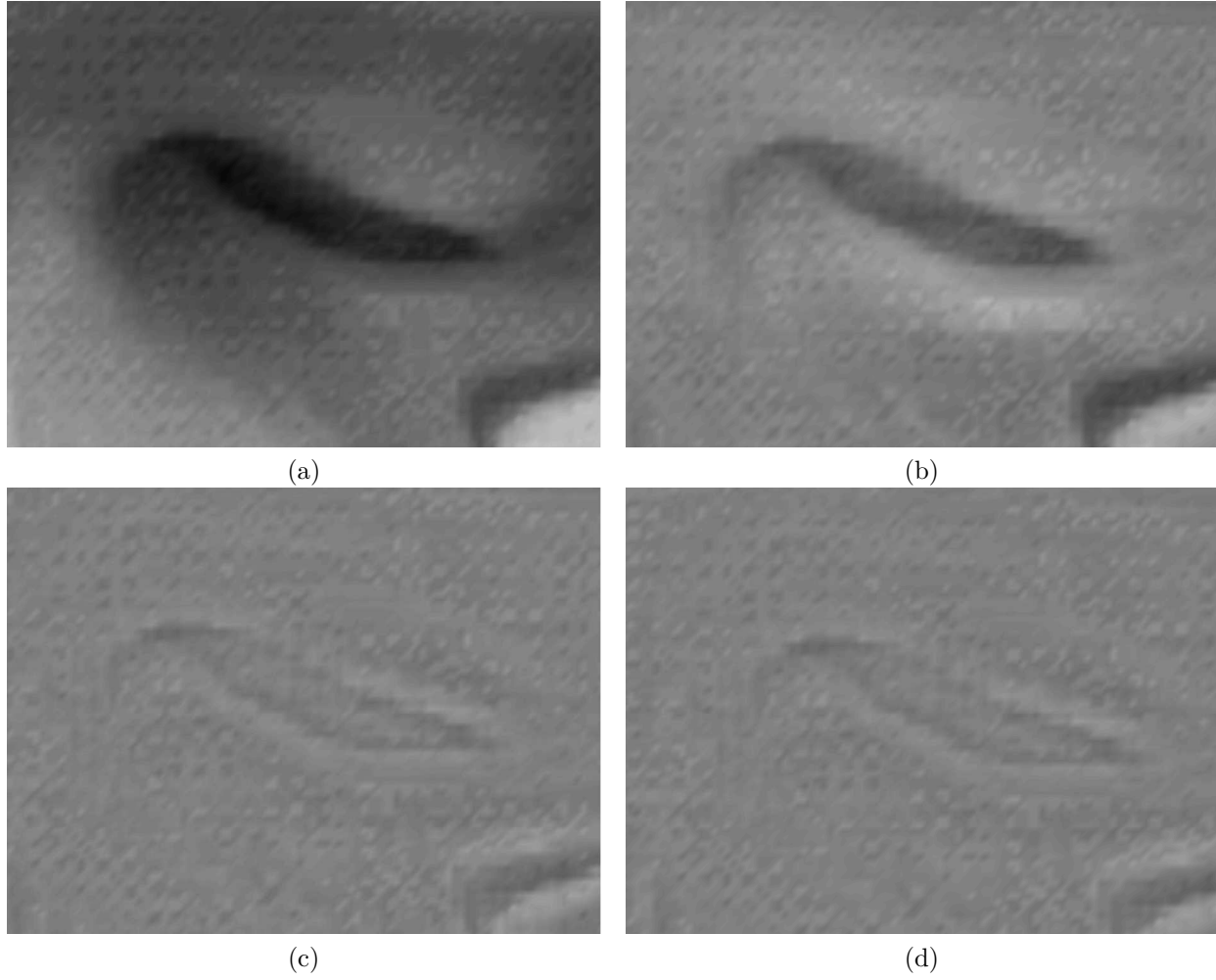
Figure 14: Close-up of Fig. 13 Edges extraction from a real video data (EU-METSAT water vapour canal) showing the evolution of a vorticity band . (a) Original video. (b) Edges extraction with wavelets. (c) Edges extraction with curvelets. (d) Edges extraction by the TV-synthesis curvelet transform
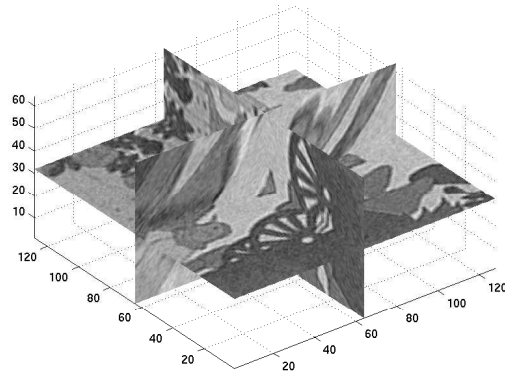
(a)
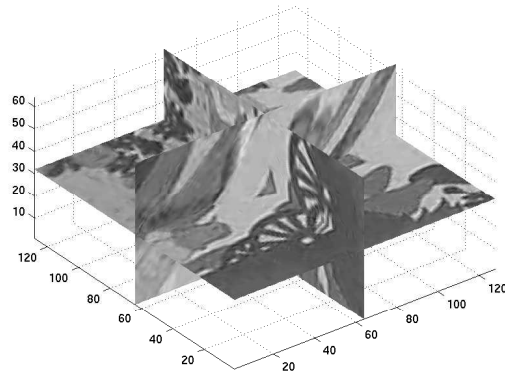
(b)
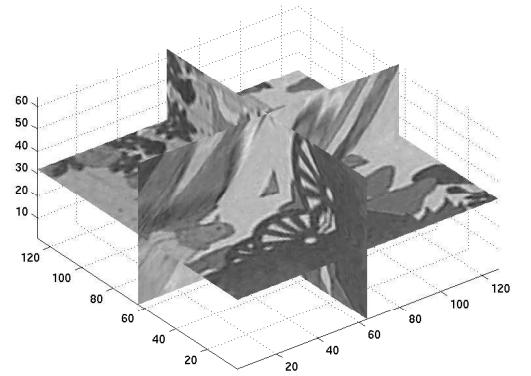
(c)

Figure 15: Denoising of a video data consisting of complex structures. (a) original video with noisy. (b) 3D wavelet denoising (SNR = 36.99). (c) 3D TV-synthesis curvelet denoising (SNR = 34.92 dB).

(a) (b) (c)
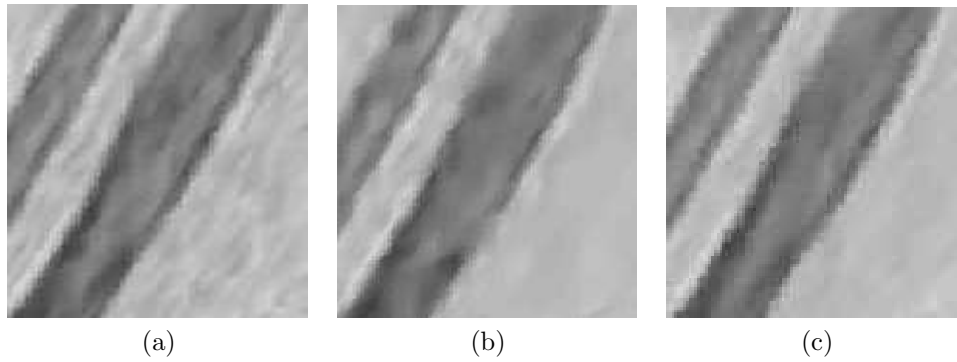
Figure 16: Close-up of Fig. 15. (a) Noisy data. (b) wavelet denoising. (c) TV-synthesis curvelet denoising.